Analytical and Experimental Investigation into the Effects of Leading-Edge Radius on Gust-Aerofoil Interaction Noise

Journal:	*Journal of Fluid Mechanics*
Manuscript ID	JFM-16-S-1470.R2
mss type:	Standard
Date Submitted by the Author:	17-Aug-2017
Complete List of Authors:	Ayton, Lorna; University of Cambridge, Applied mathematics and theoretical physics Chaitanya, Paruchuri; University of Southampton, Institute of Sound and Vibration Research
Keyword:	Aeroacoustics < Acoustics

Under consideration for publication in J. Fluid Mech.

Analytical and Experimental Investigation into the Effects of Leading-Edge Radius on Gust-Aerofoil Interaction Noise

LORNA J. AYTON †[1] and PARUCHURI CHAITANYA [2]

[1]Department of Applied Mathematics and Theoretical Physics, University of Cambridge, Wilberforce Road, CB3 0WA, UK
[2]Faculty of Engineering and the Environment, University of Southampton, Burgess Road, Southampton, SO16 7QF

(Received 17 August 2017)

This paper investigates the effects of local leading-edge geometry on unsteady aerofoil interaction noise. Analytical results are obtained by extending previous work for parabolic leading edges to leading edges of the form x^m for $0 < m < 1$. Rapid distortion theory governs the interaction of an unsteady vortical perturbation interacting with a rigid aerofoil in compressible steady mean flow that is uniform far upstream. For high-frequency gusts interacting with aerofoils of small total thickness this allows a matched asymptotic solution to be obtained. This paper mainly focusses on obtaining the analytic solution in the leading-edge inner region, which is the dominant term in determining the total far-field acoustic directivity, and contains the effects of the local leading-edge geometry. Experimental measurements for the noise generated by aerofoils with different leading-edge nose radii in uniform flow with approximate homogeneous, isotropic turbulence are also presented. Both experimental and analytic results predict that a larger nose radius generates less overall noise in low Mach number flow. By considering individual terms in the analytic solution, this paper is able to propose reasons behind this result.

1. Introduction

Aerofoil turbulence interaction noise, also commonly known as leading-edge noise, is a dominant contributor to overall levels of unwanted noise generated by aeroengines due to rotor-stator interaction (Peake & Parry 2012), and is produced due to the interaction of the wakes generated by a forward blade row with a subsequent blade row. With increasingly tight European noise regulations, such as the Flightpath 2050 target of a 65% aircraft noise reduction with respect to 2000 noise levels, it is imperative we improve our understanding of noise generation within aircrafts and develop new designs to reduce this noise.

In one of the simplest (analytic) models Sears (1941) predicts the far-field noise generated by a single flat plate interacting with an unsteady vortical gust. This is extended by Amiet (1975) to consider the effects of homogeneous isotropic turbulence interacting with a flat plate in uniform flow. Realistic geometry effects are now included in analytic solutions; Myers & Kerschen (1997) considers the effects of angle of attack and camber, Tsai (1992) considers the effects of non-zero maximum blade thickness, and Ayton (2016) combines maximum thickness, camber and angle of attack effects, thus accounting for full aerofoil geometry. In the latest analytic models (Myers & Kerschen 1997; Tsai 1992;

† Email address for correspondence: L.J.Ayton@damtp.cam.ac.uk

Ayton 2016), only high-frequency, $k \gg 1$, incident gusts are considered to allow matched asymptotic solutions to be found, and the effects of geometry are parameterised by a single constant, $\epsilon \ll 1$, which denotes the global size of the mean flow perturbation from a uniform flow (hence ϵ denotes the maximum thickness or camber of the aerofoil under consideration).

These analytic approaches use rapid distortion theory (Goldstein 1978) to separate the unsteady flow field into two parts; a convective part that describes the distortion of the gust in the mean flow, and a scattered part that contains the acoustic field due to the interaction of the distorted gust with the rigid aerofoil. Acoustic pressure is generated in two ways; the distorted vorticity acting as a source term, and the unsteady vorticity interacting with the rigid surface. One benefit of analytic solutions is that they can easily identify the effects on the far-field noise of these two different contributors.

A variety of numerical methods also consider the effects of geometry on unsteady aerofoil interaction noise (Grace 2001; Allampalli *et al.* 2009; Lockard & Morris 1998; Glegg & Devenport 2009). With regards to the effects of thickness, these use a single parameter denoting the maximum thickness of the aerofoil, and supposed the aerofoils have parabolic leading edges ($y \sim \sqrt{x}$) (as do the analytic methods Tsai (1992) and Ayton (2016)). It is found both numerically and analytically that for high-frequency interactions, increasing maximum aerofoil thickness reduces the total far field noise, which is confirmed experimentally (Olsen & Wagner 1982). There are however some contradictions between numerical and experimental results, for example Lockard & Morris (1998) find that the far-field directivity patterns skew towards the upstream direction with increasing thickness, but this is not found experimentally by Olsen & Wagner (1982). This could be due to difficulties in taking experimental measurements directly upstream of the aerofoil due to the location of the nozzle, or because the unsteady Kutta condition (Crighton 1985) is not imposed in the inviscid results presented in Lockard & Morris (1998); neglecting the unsteady Kutta condition is shown to significantly affect the upstream far-field directivity pattern (Ayton *et al.* 2016).

The idea that increased thickness can reduce high-frequency far-field noise led to investigating the effects of leading-edge nose radius on unsteady interaction noise, with experimental (Hall *et al.* 2011; Devenport *et al.* 2010; Chaitanya *et al.* 2015) and numerical (Gill *et al.* 2013) results both showing trends of a reduction of far-field noise with increased nose radius. It is proposed in Gill *et al.* (2013) that the distortions of the steady flow near the nose of the aerofoil are the primary noise reduction mechanism for increasing maximum thickness, and increasing nose radius. Typical outlet guide vane (OGV) geometries have approximately 5% thickness relative to aerofoil chord. To reduce the interaction noise, increasing the total thickness is unrealistic due to its influence on aerodynamic performance. Understanding how small changes in nose radius can lead to significant changes in far-field radiated noise is therefore key to realistically reducing aerofoil interaction noise.

In this paper we wish to improve the understanding of the effects of aerofoil leading-edge geometry on gust-aerofoil interaction noise by obtaining an analytic solution for the far-field acoustics, extending previous work based on rapid distortion theory. In particular, the analytic solution found can separate the effects of volume sources, the locally distorted mean flow, and unsteady vorticity interacting with the rigid surface, hence by considering these effects separately we aim to develop a broader understanding of the roles of each feature on noise generation. The analytic results determine trends for single-frequency unsteady upstream perturbations that are compared to the trends seen in (fully turbulent) experimental data.

In Section 2 we discuss the analytic formulation of the problem, and how to extend pre-

vious analytic results (Tsai 1992; Ayton 2016) to a more general leading-edge geometry. In Section 2.2 we solve the governing equations in a local inner region around the aerofoil nose. This region contains the key terms contributing to the overall solution that depend on the local leading-edge geometry. The experimental setup is discussed in Section 3, and results are presented in Section 4. We discuss our conclusions in Section 5.

2. Analytic Solution

We wish to find the acoustic field generated by a small unsteady vortical perturbation interacting with an aerofoil with arbitrary leading-edge geometry and chord length $2c^*$ in steady flow which far upstream is uniform $\boldsymbol{U} = U^*_\infty \boldsymbol{e}_x$ (where * denotes a dimensional quantity). From hereon in lengths are non-dimensionalised by semi-chord, c^*, and velocities by U^*_∞. The boundary of the aerofoil is denoted as $\epsilon y(x)$ such that $y(0) = y(2) = 0$ and, since we consider only thin aerofoils, we have an asymptotic parameter $\epsilon \ll 1$ governing the maximum thickness of the aerofoil. We consider leading-edge geometries $y \sim \epsilon a_0 x^m$ as $x \to 0$ for $0 < m < 1$ and a_0 a suitable $O(1)$ constant.

2.1. *Governing Equations*

Analytic solutions for high-frequency gust-aerofoil interaction noise exist in the case of a parabolic leading edge, $m = 1/2$, for both symmetric (Tsai 1992) and non-symmetric (Ayton 2016) aerofoils in steady flow that far upstream is uniform with Mach number M_∞. These are obtained by solving the rapid distortion theory equations (Goldstein 1978) governing the acoustic field. Full derivation of these equations (which are relevant still for arbitrary leading-edge geometry) can be found in Myers & Kerschen (1995, 1997), Tsai (1992) and Ayton (2016) and therefore are just quoted here. Whilst this work is valid for both symmetric and non-symmetric aerofoils, for simplicity we shall restrict the analysis to the symmetric case only, since it has been found that the effects of camber and angle of attack on aerofoil noise in isotropic turbulence are relatively small in comparison to the effects of thickness (Devenport *et al.* 2010).

As is typical in thin aerofoil interaction theory, we work in coordinate system (ϕ, ψ) which denote the potential and streamfunction of the steady mean flow, and relate to Cartesian coordinates via

$$x + i\beta_\infty y = z + \epsilon F(z), \tag{2.1}$$

where $z = \phi + \mathrm{i}\psi$, $\beta_\infty = \sqrt{1 - M^2_\infty}$ is the Prandtl-Glauert transformation factor accounting for compressibility, and F is the complex potential of the mean flow. A key benefit of this coordinate system is that the aerofoil boundary is now mapped to $\psi = 0$.

The complex potential, $F(z)$, can be found by using thin aerofoil theory (Thwaites 1960)

$$q(\phi, \psi) - i\mu(\phi, \psi) = \frac{dF}{dz}, \tag{2.2}$$

where

$$(q - i\mu)(z) = \frac{1}{\pi\beta_\infty} \int_0^2 \frac{y'(x)}{z - x} dx, \tag{2.3}$$

and the constant of integration for F is chosen such that $F(0) = 0$. The mean flow around the aerofoil in our new coordinates is therefore $(1 + \epsilon q)\boldsymbol{e}_\phi$.

We denote the convective vortical disturbance far upstream as $\nu \boldsymbol{v}_\infty = \nu(A_t, A_n, A_3) e^{ik(\phi + k_n \psi + k_3 z - t)}$, and require $A_t + A_n k_n \beta_\infty + A_3 k_3 = 0$. We set $\nu \ll \epsilon$ so that the unsteady perturbation is much smaller than the mean flow distortion due to the aerofoil, and consider a high-frequency limit, $k \gg 1$, with a distinguished scaling $\epsilon k = O(1)$, in line with all

previous analytical gust-aerofoil interaction models (Myers & Kerschen 1995, 1997; Tsai 1992; Ayton 2016). We separate the total unsteady flow field into two parts; the known evolution of the gust in the mean flow, $\nu \boldsymbol{v}_g$; and the unknown response to the interaction with the aerofoil, $\nu \boldsymbol{v}_a = \nu \nabla G$, which contains the acoustics that propagate to the far field. We suppose the flow is inviscid, non-heat conducting, and a perfect gas.

We define the modified potential as

$$h(\phi, \psi) = G \mathrm{e}^{\mathrm{i} M_\infty^2 \phi / \beta_\infty^2 - M_\infty^2 \epsilon q}, \tag{2.4}$$

hence the linearised Euler equations become

$$\frac{\partial^2 h}{\partial \phi^2} + \frac{\partial^2 h}{\partial \psi^2} + k^2 w^2 (1 - 2\beta_\infty^2 \epsilon q) h + \frac{(\gamma+1) M_\infty^4 \epsilon q}{\beta_\infty^2} \left(\frac{\partial^2 h}{\partial \psi^2} + 2ik\delta \frac{\partial h}{\partial \phi} + k^2 (w^2 + \delta^2) h \right) - \frac{(\gamma+1) M_\infty^4 \epsilon}{\beta_\infty^2} \frac{\partial q}{\partial \phi} \left(\frac{\partial h}{\partial \phi} - ik\delta h \right) = k\epsilon S(\phi, \psi) e^{ik\Omega}, \tag{2.5a}$$

where

$$\delta = 1/\beta_\infty^2, \qquad w^2 = (M_\infty \delta)^2 - (k_3/\beta_\infty)^2, \qquad \Omega = \delta\phi + k_n \psi + \epsilon g(\phi, \psi), \tag{2.5b}$$

and the forcing arising from $\boldsymbol{v}_g$ is

$$S(\phi, \psi) = \frac{2}{\beta_\infty^2} \left(i(A_t - A_n k_n \beta_\infty^3) q + i(\beta_\infty^2 k_n A_t + A_n \beta_\infty) \mu + \frac{A_t M_\infty^2}{k} \frac{\partial q}{\partial \phi} + \frac{A_n M_\infty^2 \beta_\infty}{k} \frac{\partial q}{\partial \psi} \right). \tag{2.5c}$$

The function, $g(\phi, \psi)$, is Lighthill's drift function,

$$g(\phi, \psi) = -2 \int_{-\infty}^{\phi} q(\eta, \psi) d\eta, \tag{2.5d}$$

and the boundary condition of zero normal velocity on the aerofoil surface is given by

$$\left. \frac{\partial h}{\partial \psi} + M_\infty^2 \epsilon \frac{\partial q}{\partial \psi} h \right|_{\psi=0} = \left. \left(-\frac{A_n}{\beta_\infty} + 2\epsilon\mu A_t + \frac{A_n M_\infty^2 \epsilon q}{\beta_\infty} \right) e^{ik\Omega} \right|_{\psi=0}. \tag{2.6}$$

Pressure is obtained from the modified potential via

$$p = -\left(\frac{\partial h}{\partial \phi} - ik\delta h \right) e^{-ik\delta M_\infty^2 \phi}. \tag{2.7}$$

which is derived in Myers & Kerschen (1995, eq. (2.7)).

The method of matched asymptotic expansions (Van Dyke 1975) is used to solve (2.5a) subject to (2.6). There are five regions of interest; inner regions around the leading and trailing edges, transition regions above the rigid surfaces and wake, and an outer region. These are depicted in Figure 1. For aerofoils with parabolic leading edges, $y \sim \sqrt{x}$ as $x \to 0$, the solution in all regions can be found in Ayton (2016).

For high-frequency gusts, it is known that the leading-edge inner solution is dominant in determining the far-field acoustic pressure (Tsai 1992). The trailing-edge inner region produces an acoustic field that propagates to the outer region and acts predominantly to enforce a continuity of pressure and velocity across the trailing edge via a Kutta condition. This trailing-edge solution is $O(k^{-1/2})$ smaller than the leading-edge inner solution and propagates with a phase shift compared to the leading-edge solution thus modulates the total far-field directivity. The transition solutions do not propagate acoustics to the far field except at small downstream angles $\theta = O(k^{-1/2})$. Therefore if we wish to determine the effects of altering the leading-edge geometry on the far-field noise it is sufficient to

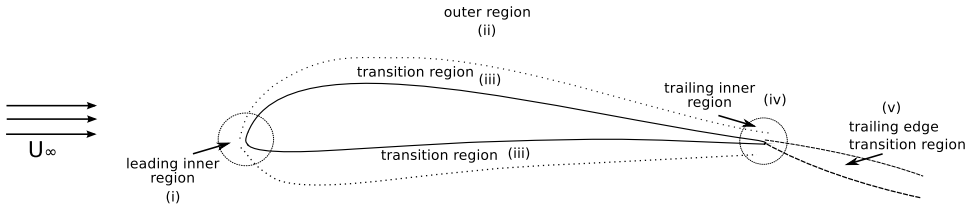

(a) In (x, y) space.

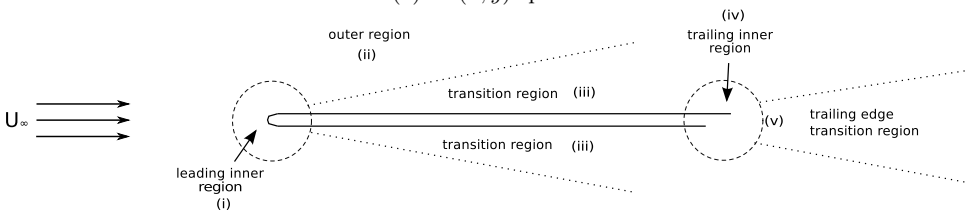

(b) In (ϕ, ψ) space.

Figure 1: Asymptotic regions around the aerofoil; leading- and trailing-edge inner regions, (i) and (iv); transition regions, (iii) and (v); and the outer region, (ii).

.

consider the leading-edge inner region at $O(1)$+first-order correction (the size of which will be discussed in the next section) in Sections 2.2 and 2.3, and the trailing-edge inner region at $O(k^{-1/2})$ (which is the leading-order term of the trailing-edge inner solution) in Section 2.4. We must also account for the distortion of the inner solutions as they propagate noise to the far field, which is discussed in Section 2.5.

2.2. *Leading-Edge Inner Region*

In the leading-edge inner region, (i) in Figure 1, we use leading-edge inner variables $(\Phi, \Psi) = k(\phi, \psi)$, and define the leading-edge inner potential as $H(\Phi, \Psi)$. The governing equation becomes

$$\frac{\partial^2 H}{\partial \Phi^2} + \frac{\partial^2 H}{\partial \Psi^2} + w^2(1 - 2\beta_\infty^2 \epsilon q)H + \frac{(\gamma+1)M_\infty^4}{\beta_\infty^2}\epsilon q\left(\frac{\partial^2 H}{\partial \Psi^2} + 2i\delta\frac{\partial H}{\partial \Phi} + (w^2+\delta^2)H\right) - \frac{(\gamma+1)M_\infty^4}{\beta_\infty^2}\epsilon\frac{\partial q}{\partial \Phi}\left(\frac{\partial H}{\partial \Phi} - i\delta H\right) = \frac{\epsilon}{k}e^{i\bar{\Omega}}S(\Phi, \Psi), \quad (2.8a)$$

$$\bar{\Omega} = \delta\Phi + k_n\Psi + k\epsilon g(\Phi, \Psi), \quad (2.8b)$$

$$S(\Phi, \Psi) = \frac{2}{\beta_\infty^2}\left(iq(A_t^* - A_n k_n \beta_\infty^3) + i\beta_\infty\mu(\beta_\infty k_n A_t^* + A_n) + A_t^* M_\infty^2\frac{\partial q}{\partial \Phi} + A_n M_\infty^2 \beta_\infty \frac{\partial q}{\partial \Psi}\right), \quad (2.8c)$$

and the boundary condition becomes

$$\frac{\partial H}{\partial \Psi} + M_\infty^2 \epsilon \frac{\partial q}{\partial \Psi} H\bigg|_{\Psi=0\pm} = \frac{1}{k}\left(-\frac{A_n}{\beta_\infty} + 2\epsilon\mu A_t^* + \frac{A_n M_\infty^2 \epsilon q}{\beta_\infty}\right)e^{i\bar{\Omega}}\bigg|_{\psi=0}, \quad (2.9)$$

for $\Phi > 0$.

The inner governing equation and boundary condition contain small terms of size $O(\epsilon q)$. To determine the asymptotic scaling parameter required in the inner region we need to determine the scaling of these small terms. Therefore we consider (2.3) for inner

variable $Z = kz$ to find

$$q - \mathrm{i}\mu \sim \epsilon a_0 k^{1-m} \frac{m}{Z^{1-m}\beta_\infty}(-1)^m \csc(m\pi) + O(\epsilon k^{-m}). \tag{2.10}$$

Note this is singular at $m = 1$ since thin aerofoil theory is not appropriate for a sharp wedge $y \sim x$. We find $q = O(\epsilon k^{1-m}) \times O(m/\sin(m\pi))$, which is $O(\epsilon k^{1-m})$ for $0 < m \lesssim 0.8$, therefore we shall restrict our attention to values of m such that $0 < m < 0.8$, to avoid unnecessary complexity of the asymptotic scaling parameter.

We therefore seek a solution

$$H(\Phi, \Psi) = \frac{1}{k} e^{2ik\epsilon F(-\infty)} \left(H_0 + \epsilon k^{1-m}(H_1 + H_2 + H_3) \right), \tag{2.11}$$

The $O(\epsilon k^{1-m})$ term is separated into three components as done for the parabolic ($m = 1/2$) leading-edge cases (Tsai 1992; Ayton 2016). The separate terms correspond to different physical mechanisms which will be discussed as we present analysis for each term.

2.2.1. *Solution for H_0*

This is as if we had a gust impinging on a semi-infinite flat plate, and corresponds to the effects of blocking the vertical gust velocity components. We must solve

$$D(H_0) = 0, \tag{2.12a}$$

$$\left.\frac{\partial H_0}{\partial \Psi}\right|_{\substack{\Phi>0 \\ \Psi=0}} = -\frac{A_n}{\beta_\infty} e^{i\delta\Phi}, \tag{2.12b}$$

where D is the Helmholtz operator defined by $D = \frac{\partial^2}{\partial \Phi^2} + \frac{\partial^2}{\partial \Psi^2} + w^2$. We solve using the Wiener-Hopf method, obtaining

$$H_0 = -\frac{A_n \operatorname{sgn}(\Psi)}{\beta_\infty 2\pi\sqrt{\delta + w}} \int_{-\infty}^{\infty} \frac{e^{-i\lambda\Phi - |\Psi|\sqrt{\lambda^2 - w^2}}}{(\lambda + \delta)\sqrt{\lambda + w}} d\lambda. \tag{2.13}$$

To covert back to (ϕ, ψ) variables from leading-edge variables, (Φ, Ψ), we take an outer limit and use the method of steepest descents (Bender & Orszag 1978). The saddle point is at $\lambda = -w\cos\theta$, yielding

$$H_0 \sim L_0(\theta) \frac{e^{ikwr}}{\sqrt{kr}} + O(k^{-3/2}), \tag{2.14a}$$

$$L_0(\theta) = -\frac{A_n e^{-i\pi/4} \cos\theta/2}{\beta_\infty \sqrt{\pi}\sqrt{\delta + w}(\delta - w\cos\theta)}, \tag{2.14b}$$

This flat-plate solution is discussed in detail in Tsai (1992). The outer limit, (2.14), represents the acoustic field propagating from the inner region to the outer region, and provides a directivity function, $L_0(\theta)$, for the acoustic pressure in the outer region.

2.2.2. *Solution for H_1*

This solution takes account of the effects of thickness on the boundary condition, due to changing of the surface normal direction. We must solve

$$D(H_1) = 0, \tag{2.15a}$$

$$\left.\frac{\partial H_1}{\partial \Psi}\right|_{\substack{\Phi>0\\ \Psi=0\pm}} = \frac{\mathrm{sgn}(\Psi)}{\pi\beta_\infty}\Gamma(1-m)\Gamma(1+m)\left[2A_t^*\sin(m\pi) - \frac{A_n M_\infty^2}{\beta_\infty}\cos(m\pi)\right]\frac{e^{i\delta\Phi}}{\Phi^{1-m}} \tag{2.15b}$$

$$\equiv \mathrm{sgn}(\Psi)\mathcal{C}(m)\frac{e^{i\delta\Phi}}{\Phi^{1-m}}. \tag{2.15c}$$

This yields

$$H_1 = -\frac{\mathcal{C}(m)\Gamma(m)(-\mathrm{i})^{-m}}{2\pi}\int_{-\infty}^{\infty}\frac{e^{-i\lambda\Phi-|\Psi|\sqrt{\lambda^2-w^2}}}{\sqrt{\lambda^2-w^2}(\lambda+\delta)^m}d\lambda, \tag{2.16}$$

which has outer limit

$$H_1 \sim L_1(\theta)\frac{e^{ikwr}}{\sqrt{kr}} + O(k^{-3/2}), \tag{2.17a}$$

$$L_1(\theta) = \frac{\mathrm{i}\,\Gamma(m)\mathcal{C}(m)\mathrm{e}^{-\pi\mathrm{i}/4}\mathrm{e}^{\pi\mathrm{i}m/2}}{\sqrt{2\pi w}(\delta - w\cos\theta)^m}. \tag{2.17b}$$

2.2.3. *Solution for H_2*

We now take account of the volume source in (2.8), arising from the distortion of the incident gust in the locally non-uniform flow at the leading edge. We must solve

$$D(H_2) = \mathrm{e}^{\mathrm{i}\delta\Phi+\mathrm{i}k_n\Psi}\left(\frac{C_1}{R^{1-m}}\cos\left[(1-m)\theta+m\pi\right] + \frac{C_2}{R^{1-m}}\sin\left[(1-m)\theta+m\pi\right]\right.$$
$$\left. + \frac{C_3}{R^{2-m}}\cos\left[(2-m)\theta+m\pi\right] + \frac{C_4}{R^{2-m}}\sin\left[(2-m)\theta+m\pi\right]\right) \tag{2.18a}$$

$$\left.\frac{\partial H_2}{\partial \Psi}\right|_{\substack{\Phi>0\\ \Psi=0\pm}} = 0 \tag{2.18b}$$

where

$$C_1 = \frac{2iC}{\beta_\infty^2}(A_t^* - A_n k_n \beta_\infty^3), \qquad C_2 = -\frac{2iC}{\beta_\infty}(A_n + k_n A_t^*\beta_\infty),$$
$$C_3 = -\frac{CA_t^* M_\infty^2(1-m)}{\beta_\infty^2}, \qquad C_4 = -\frac{2CA_n M_\infty^2}{\beta_\infty}, \tag{2.18c}$$

with $C = \Gamma(1-m)\Gamma(1+m)a_0/(\pi\beta_\infty)$.

We follow the same procedure as the parabolic leading-edge cases (Tsai 1992; Ayton 2016); we split the solution into a particular solution, H_{2p} that solves for the forcing in the governing equation, and a complementary solution, H_{2c}, that then enforces the correct boundary condition. We solve for H_{2p} by taking Fourier transforms in both the

Φ and Ψ variables yielding;

$$H_{2p}(\Phi,\Psi) = \frac{-\mathrm{e}^{-\pi \mathrm{i} m/2}(1-\mathrm{e}^{2\pi \mathrm{i} m})\Gamma(m)}{16\pi(1-m)(\delta^2+k_n^2)} \int_{-\infty}^{\infty} \left(\frac{(\delta+\lambda)f_1(\lambda) + ik_n\, f_2(\lambda)}{\sqrt{\lambda^2-w^2}} - \mathrm{sgn}(\Psi) f_2(\lambda) \right) \frac{\mathrm{e}^{a(\lambda,\Phi,\Psi)} d\lambda}{(\lambda+\delta)^m(\lambda-\lambda_1)(\lambda-\lambda_2)} + \frac{\mathrm{e}^{\mathrm{i}k_n\Psi}\mathrm{e}^{-\pi \mathrm{i} m/2}(1-\mathrm{e}^{2\pi \mathrm{i} m})\Gamma(m)}{16\pi(1-m)(\delta^2+k_n^2)} \int_{-\infty}^{\infty} \left(\frac{f_1(\lambda)}{(\lambda+\delta')^m} - \frac{\mathrm{sgn}(\Psi) f_2(\lambda)}{(\lambda+\delta)^m} \right) \frac{e^{h(\lambda,\Phi,\Psi)} d\lambda}{(\lambda-\lambda_1)(\lambda-\lambda_2)}, \tag{2.19a}$$

where

$$f_1(\lambda) = \left[C_1(m-1) - \mathrm{i}(\delta+\lambda)C_3\right](-k_n^2+w^2+\delta^2+2\delta\lambda) + 2(\delta+\lambda)k_n\left[C_2(m-1) - \mathrm{i}(\delta+\lambda)C_4\right], \tag{2.19b}$$

$$f_2(\lambda) = \left[C_2(m-1)\mathrm{i} + (\delta+\lambda)C_4\right](k_n^2-w^2-\delta^2-2\delta\lambda) + 2(\delta+\lambda)k_n\left[\mathrm{i}C_1(m-1) + (\delta+\lambda)C_3\right], \tag{2.19c}$$

$$\lambda_{1,2} = -\frac{\delta}{2}\left(\frac{\delta^2+k_n^2+w^2}{\delta^2+k_n^2}\right) \pm \frac{ik_n}{2}\left(\frac{\delta^2+k_n^2-w^2}{\delta^2+k_n^2}\right). \tag{2.19d}$$

The acoustic phase is

$$a(\lambda,\Phi,\Psi) = -i\lambda\Phi - |\Psi|\sqrt{\lambda^2-w^2}, \tag{2.19e}$$

and the hydrodynamic phase is

$$h(\lambda,\Phi,\Psi) = -i\lambda\Phi - |\Psi|\sqrt{(\lambda+\delta)(\lambda+\delta')}. \tag{2.19f}$$

For convergence, δ is assumed to have a small positive imaginary part, and δ' has a corresponding small negative imaginary part.

We notice two types of solution; an acoustic and a hydrodynamic solution. It is only the acoustic field that will provide pressure fluctuations in the far field. The key functional difference between our solution for a general leading-edge geometry and that for a parabolic leading edge is the $(\lambda+\delta)^m$ poles present in both acoustic and hydrodynamic terms. We can therefore obtain the complementary solution from previous work that assumes $m = 1/2$ (Tsai 1992; Ayton 2016) by making the relevant changes to these pole terms;

$$H_{2c}(\Phi,\Psi) = \frac{-\mathrm{sgn}(\Psi)\mathrm{e}^{-\pi \mathrm{i} m/2}(1-\mathrm{e}^{2\pi \mathrm{i} m})\Gamma(m)}{16\pi(1-m)(\delta^2+k_n^2)} \int_{-\infty}^{\infty} \Bigg\{ 2(-\delta C_4 + k_n C_3)\mathcal{H}(\frac{1}{2}-m) - \left(\frac{\sqrt{\lambda+w}\, f_2(\lambda)}{(\lambda+\delta)^m(\lambda-\lambda_2)} + \frac{\sqrt{\lambda_1+w}\, f_2(\lambda_1)}{(\lambda_1+\delta)^m(\lambda_1-\lambda_2)} \right) \frac{1}{\lambda-\lambda_1} + \frac{(\lambda_2+\delta)f_2(\lambda_2) + ik_n f_1(\lambda_2)}{\sqrt{\lambda_2-w}(\lambda_2+\delta')^m(\lambda_2-\lambda)(\lambda-\lambda_1)} \Bigg\} \frac{e^{a(\lambda,\Phi,\Psi)}}{\sqrt{\lambda+w}} d\lambda. \tag{2.19g}$$

This is obtained using the Wiener-Hopf method, with the Heaviside function, $\mathcal{H}$ (defined such that $\mathcal{H}(0) = 1/2$), occurring due to the entire function arising from Liouville's theorem. The outer limit, $L_2(\theta)\mathrm{e}^{\mathrm{i}kwr}/\sqrt{kr}$, for the acoustic contributions can be obtained using steepest descents as before, and is given in Appendix A.

2.2.4. *Solution for H_3*

The final term to be found in our leading-edge inner solution arises due to the distortion of the zeroth-order term, H_0, as it interacts with the locally non-uniform mean flow

around the nose of the aerofoil. We must solve

$$D(H_3) = 2\beta_\infty^2 w^2 q H_0 - \frac{(\gamma+1)M_\infty^4}{\beta_\infty^2} q\left(\frac{\partial^2 H_0}{\partial \Psi^2} + 2\mathrm{i}\delta\frac{\partial H_0}{\partial \Phi} + (w^2+\delta^2)H_0\right) + \frac{(\gamma+1)M_\infty^4}{\beta_\infty^2}\frac{\partial q}{\partial \Phi}\left(\frac{\partial H_0}{\partial \Phi} - \mathrm{i}\delta H_0\right), \tag{2.20a}$$

$$\left.\frac{\partial H_3}{\partial \Psi}\right|_{\substack{\Phi>0\\ \Psi=0\pm}} = -M_\infty^2 \frac{\partial q}{\partial \Psi} H_0. \tag{2.20b}$$

We solve by splitting the solution into a particular, H_{3p}, and a complementary solution, $H_{3c} = H_{3c_1} + H_{3c_2} + H_{3c_3}$, as for the parabolic case. The solutions can be found in the Appendix B along with their outer limits, $L_{3p}(\theta)\mathrm{e}^{\mathrm{i}kwr}/\sqrt{kr}$ and $L_{3c_{1,2,3}}(\theta)\mathrm{e}^{\mathrm{i}kwr}/\sqrt{kr}$.

2.3. *Outer limit of the leading-edge inner solution*

We have now completed the solution for the leading-edge inner region which is dominant in determining the effects of leading-edge geometry on the far-field acoustics. To summarise, the outer limit of the leading-edge inner solution yields

$$h_l(r,\theta) \sim \frac{\mathrm{e}^{\mathrm{i}kwr + 2\mathrm{i}k\epsilon F(-\infty)}}{k^{3/2}\sqrt{r}}\left(L_0(\theta) + \epsilon k^{1-m}\left[L_1(\theta) + L_2(\theta) + L_{3p}(\theta) + L_{3c_1}(\theta) + L_{3c_2}(\theta) + L_{3c_3}(\theta)\right]\right) \tag{2.21a}$$

$$= \frac{\mathrm{e}^{\mathrm{i}kwr + 2\mathrm{i}k\epsilon F(-\infty)}}{\sqrt{kr}} D_l(\theta), \tag{2.21b}$$

which gives the leading-edge directivity function, $D_l(\theta)$, correct to $O(\epsilon k^{1-m})$, generated by interactions at the leading edge. Note the phase function, $2\mathrm{i}k\epsilon F(-\infty)$, and additional amplitude multiplier, k^{-1}, have arisen due to the proposed form of the leading-edge inner solution, (2.11).

We can use this solution, (2.21), to investigate the effects of altering the leading-edge geometry on the far-field acoustics, in particular, the different contributions to the solution can highlight the effects of different physical processes.

2.4. *Trailing-edge solution*

Here we discuss the solution in region (iv) of Figure 1.

Trailing-edge coordinates are defined as (ϕ_t, ψ_t), where

$$\phi = 2 + \alpha_t + \phi_t, \qquad \psi = \psi_t, \tag{2.22}$$

with $\alpha_t = \mathrm{Re}(\epsilon F(2))$. The inner acoustic potential is labelled $H_t(\Phi_t, \Psi_t)$, where $(\Phi_t, \Psi_t) = k(\phi_t, \psi_t)$ are trailing-edge inner coordinates.

We wish to find only the leading-order contribution to the trailing-edge inner acoustic solution (in region (iv) of Figure 1) which is $O(k^{-1/2})$ smaller than the leading-edge inner solution. The total trailing-edge inner acoustic solution arises from the rescattering of the leading-edge acoustic field by the sharp trailing edge. If we wish to retain only the first term, we only need to consider the rescattering of the leading-order leading-edge solution, i.e. the flat plate term associated to H_0. This is independent of nose geometry, and thus we can use the solution derived in previous work (Tsai 1992; Myers & Kerschen 1995, 1997; Ayton 2016).

We therefore have an outer limit of the trailing-edge inner solution given by

$$h_t \sim \frac{\mathrm{sgn}(\psi)e^{ikwr_t}\Delta p}{\sqrt{2r_t}k^2(\delta-w)}\left(\frac{e^{\pi i/4}|\sin\theta_t/2|}{\sqrt{\pi w}(\delta-w\cos\theta_t)}+\sqrt{k}\,\mathrm{i}\mathrm{e}^{-2\mathrm{i}kw(1-\cos\theta)}\mathrm{erfc}\left[e^{-\pi i/4}\sqrt{2kw(1-\cos\theta)}\right]\right) \tag{2.23}$$

$$= \frac{\mathrm{e}^{\mathrm{i}kwr_t}}{k^2\sqrt{r_t}}D_t(\theta_t), \tag{2.24}$$

where Δp denotes the leading-order pressure jump across the trailing edge due to the leading-edge acoustic solution,

$$\Delta p = \sqrt{2}\mathrm{i}(\delta-w)L_0(0)\mathrm{e}^{\mathrm{i}k(w-\delta M_\infty^2)(2+\alpha_t)+2\mathrm{i}k\epsilon F(-\infty)}. \tag{2.25}$$

The phase terms arise in (2.25) due to the shift of coordinates from the leading edge to the trailing edge, recalling that pressure, defined by (2.7), contains additional phase factors. D_t is the trailing-edge directivity function.

2.5. *Solution in the outer region*

To construct an approximate solution in the outer region, (ii) in Figure 1, we must account for phase differences in the leading- and trailing-edge acoustic solutions. Both solutions will undergo a phase distortion as they propagate from the inner regions to the far field, and there will be a further phase shift between the two solutions due to the differing positions of the leading and trailing edges. These phase effects are not a result of the precise geometry of the nose, hence we can recover these effects directly from Tsai (1992); Ayton (2016).

The asymptotic solution for the far-field acoustics, correct to $O(k^{-3/2}\epsilon k^{1-m}, k^{-2})$, is hence given by

$$h(r,t) \sim \frac{\mathrm{e}^{\mathrm{i}kwr}}{k^{3/2}\sqrt{r}}\left(D_l(\theta)+\frac{1}{\sqrt{k}}D_t(\theta)\mathrm{e}^{ikw\sigma_s}\right) \tag{2.26}$$

where the phase shift is given by

$$\sigma_s = V(\theta)\alpha_t\cos\theta+\alpha_t\cos\theta-2\epsilon F(-\infty), \tag{2.27}$$

with

$$V(\theta) = -\frac{1}{2w}\left(2\beta_\infty^2w^2-\frac{(\gamma+1)M_\infty^4}{\beta_\infty^2}(\delta-w\cos\theta)^2\right). \tag{2.28}$$

The last two terms in (2.27) arise due to the different positions of the leading and trailing edges, whilst the first term arises because of the (relative) distortion of the inner acoustics as they propagate to the far field. We define the far-field directivity, $D(\theta)$ as

$$D(\theta) = \left(D_l(\theta)+\frac{1}{\sqrt{k}}D_t(\theta)\mathrm{e}^{ikw\sigma_s}\right). \tag{2.29}$$

3. Experimental Setup and Procedure

We shall compare our analytical solution for a single high-frequency vortical perturbation interacting with a leading edge of variable nose radius to experimental results measuring the far-field noise generated by such aerofoils in a fully turbulent stream. In this section we discuss the test facility, specific experimental setup, and extraction of results. Further details can be found in Chong *et al.* (2008) and Narayanan *et al.* (2015).

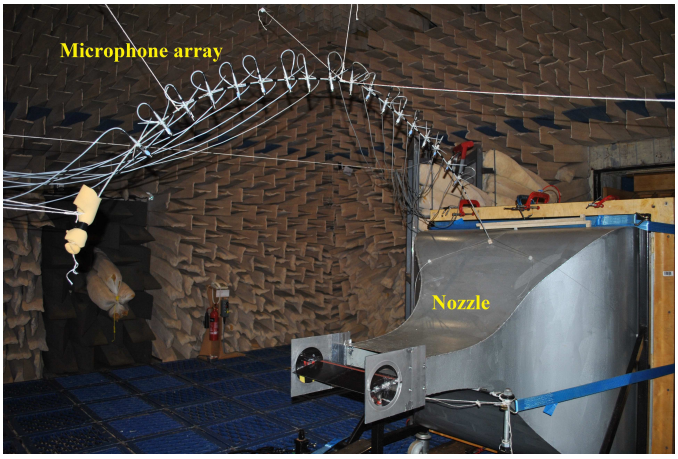

Figure 2: Photograph of jet nozzle and test setup inside the ISVR anechoic chamber.

3.1. *Open jet test facility and instrumentation*

Far-field noise measurements were carried out at the ISVR's open-jet wind tunnel facility. Figure 2 shows a photograph of the facility within the anechoic chamber of dimensions 8 m × 8 m × 8 m. The walls are acoustically treated with glass wool wedges and the cut-off frequency of the chamber is about 80Hz. The nozzle is designed as a three-dimensional, 25:1 CR nozzle. The inlet of the nozzle is a square section measuring 1.3 m x 1.3 m and the outlet is rectangular shape measuring 0.15 m x 0.45 m. The axial length of the nozzle is 1.35 m. To maintain two-dimensional flow around the aerofoil, side plates are mounted to the nozzle exit which also support the aerofoil. The nozzle dimensions are 15 cm x 45 cm. Aerofoils are located 0.15 m downstream of the nozzle to ensure that the entire aerofoil is located well within the jet potential core, whose width is at least 0.12m, as shown in figure 11a in Chong *et al.* (2008). Chong *et al.* (2008) also shows that the flow is two dimensional (no spanwise variation) to within a deviation of about 4%. The maximum jet speed investigated in this study is 80 m s^{-1}.

3.2. *Far-field noise measurements*

Free-field noise measurements are made using 11, half-inch condenser microphones (B&K type 4189) located at a constant radial distance of 1.2 m from the mid span of the aerofoil leading edge. These microphones are placed at emission angles of between 40° and 140° measured relative to the downstream jet axis. Measurements are carried out for a duration of 10 seconds at a sampling frequency of 50 kHz, and the noise spectra are calculated with a window size of 1024 data points corresponding to a frequency resolution of 48.83 Hz and a BT product of about 500, which is sufficient to ensure negligible variance in the spectral estimate.

The acoustic pressure at the microphones is recorded at the mean flow velocities of 20, 40, 60 and 80 m s^{-1} at the exit of the jet nozzle. Details of the calculation method for deducing the Sound Pressure Level spectra SPL, and the Sound Power Level spectra PWL as functions of frequency, k, are presented in Narayanan *et al.* (2015).

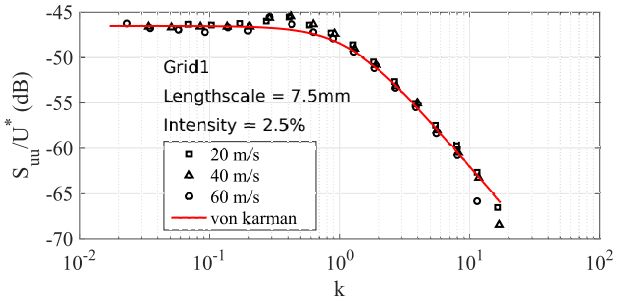

Figure 3: Comparison between the measured axial velocity spectra and theoretical von-Karman spectra.

3.3. *Turbulence characterization*

A bi-planar rectangular grid with overall dimensions of 0.63 x 0.69 m^2 located in the contraction section of the nozzle is used to generate turbulence that is closely homogeneous and isotropic. This bi-planar grid is designed based on empirical equations presented in Roach (1987) and Hinze (1959). The grid is located 0.75 m upstream of the nozzle exit. The streamwise velocity spectrum is measured using a hot wire at a single on-axis position 0.145 m down- stream from the nozzle exit. It is found to be in close agreement with the von-Karman spectrum for homogeneous and isotropic turbulence with a 2.5% turbulence intensity and a 7.5 mm integral length scale. The turbulence integral length scale is obtained by matching the theoretical spectra to the measured streamwise velocity spectra and dividing by two, assuming perfect isotropic turbulence. A comparison of the two measured streamwise velocity spectra (S_{uu}/U^*) plotted against non-dimensional frequency k together with the theoretical von-Karman spectra are plotted in figure 3, where close agreement is observed.

3.4. *3D Aerofoil models*

In this study, six NACA symmetric aerofoils are produced using 3D printing technology. We systematically vary thickness and nose radius of the aerofoils as shown in Figure 4. In the case of the NACA 4-digit aerofoils, the leading edge nose radius R_e is related to maximum thickness by

$$R_e = 0.5\left[0.2969\frac{\epsilon}{0.2}\left(\frac{I}{6}\right)\right]^2 \tag{3.1}$$

where I is a non-dimensional parameter that defines the shape of the leading edge as described in (Gill *et al.* 2013). $I = 0$, represents a sharp leading edge, represented as NACA xxxx-03, whereas $I = 10$ represents blunt aerofoils, represented as NACA xxxx-103 and $I = 6$ represents standard NACA profile geometries. Recall the analytic description of the leading edge is $y \sim \epsilon a_0 x^m$ where m and a_0 are used to alter the leading edge radius. The values of I used experimentally correspond to values and m and a_0 as given in Table 1.

In order to prevent tonal noise generation due to Tollmien-Schlichting waves convecting in the laminar boundary layer, and to ensure complete consistency between the different cases, the flow near the leading edge of the aerofoil is tripped to force transition to turbulence using a rough band of tape of width 0.0125 m located 16.6% of chord from

ϵ	I	m	a_0
0.06	0	0.83	2.3
0.06	6	0.44	1.1
0.06	10	0.32	0.95
0.12	0	0.83	2.3
0.12	6	0.44	1.1
0.12	10	0.32	0.96

Table 1: Table of values of m and a_0 that correspond to $I = 0, 6, 10$ for NACA aerofoils with maximum thickness of 6% or 12%

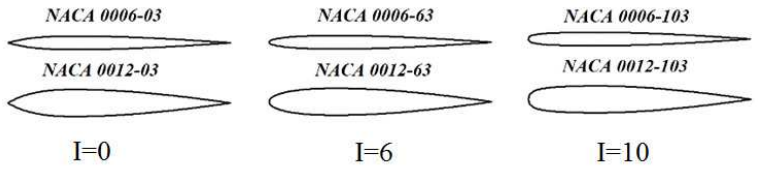

Figure 4: Symmetric aerofoil geometries considered in the study

the leading edge, on both suction and pressure sides. The tape has roughness of SS 100, corresponding to a surface roughness of 140 μ m. Transition is forced by the use of trip tape, which is many orders of magnitude rougher than the aerofoil surface, and is therefore highly unlikely to affect transition. Previous noise measurements in the facility have indicated that self-noise is insensitive to the method of tripping.

4. Results

In this section we investigate the effects of altering the leading-edge geometry on the far-field acoustic pressure solution found both analytically and experimentally. We first validate the analytical solution by showing it agrees with the experimental findings in Section 4.1, then in Section 4.2 we use the analytical solution to decompose the acoustic flow field to investigate the different physical processes happening at the aerofoil leading edge, and what the effects of altering nose radius are on these.

4.1. *Comparison of Experimental and Analytical Results*

We first compare the analytical and experimental results for the set of test cases given in Table 1. In Figure 7 we present results for the measured acoustic sound pressure levels at each of the 11 microphone locations, for aerofoils with 6% or 12% thickness that are modified forms of standard NACA 4-digit aerofoils, with leading-edge nose radii described by (3.1). Two low Mach number mean flow velocities are used corresponding to $U^* = 20, 80ms^{-1}$ ($M = 0.06, 0.24$), and two non-dimensionalised frequencies, $k = 2.5, 5$.

The total noise radiated by the aerofoil located within a turbulent flow is dominated by leading-edge noise at these chosen frequencies but by trailing-edge noise at higher frequencies. As it is very difficult to measure leading-edge noise and trailing-edge self-noise separately, our experimental analysis was limited to the frequency region where the interaction noise dominates trailing-edge self-noise. Figure 5 shows the influence of self-noise on the total noise spectra. The spectra of radiated noise due to trailing-edge self-noise

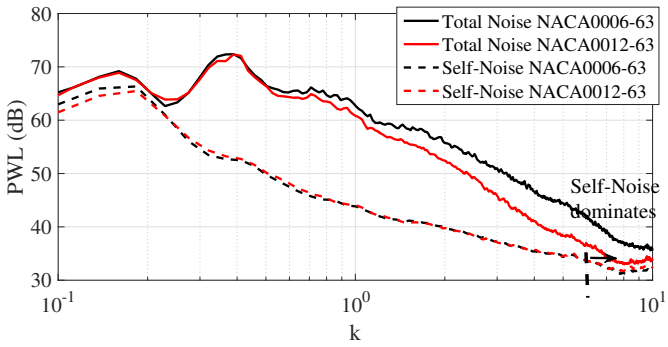

Figure 5: The Influence of Self-Noise on Total noise for 6% and 18% thickness to chord at jet velocity of 60 ms^{-1} ($M = 0.18$).

alone is obtained by removing the turbulence grid. Sound power levels are plotted against a non-dimensional frequency (k) for aerofoils with two different thicknesses for highest flow speed of $M = 0.24$. It is observed that the thicker aerofoil has lower interaction noise and the self-noise starts dominating the total noise at a relatively lower frequency compared to the thinner aerofoil. The non-dimensional frequency (k) where self-noise starts to dominant the total noise for NACA0012 is around 6. Whereas for NACA0006 it is greater than 10. These frequencies are function of incoming turbulence intensity, where in our present study it is about 2.5%. Below these frequencies the difference between total noise and trailing-edge self-noise is greater than 5dB suggesting the dominance of trailing-edge noise on total noise is negligible. Hence in the frequency range considered in this present study, leading-edge noise is the main contributor to the total far-field noise measured.

For the highest frequency, $k = 5$, and 12% thickness we see in Figure 7 that as nose radius increases (I increases), the magnitude of the acoustic pressure decreases. The level of reduction is decreased for the higher mean flow. It is known from Chaitanya *et al.* (2015) that the ratio of nose radius, R_e (which contains both ϵ and I dependence), to the hydrodynamic wavelength, U^*/k^*, is an important factor and defines the extent of gust distortion which in turn governs the far-field noise. With the increase of jet velocity, we observe a decrease in k^*R_e/U^* resulting in decrease in level of noise reduction. For a thinner overall aerofoil, 6% thickness we see the same trends to the 12%-thickness aerofoils, although the reduction in magnitude of the overall SPL is lower for an aerofoil of 6% thickness than 12% thickness. At lower frequencies $k = 2.5$ the trend continues; aerofoils with larger nose radii generate less far-field noise, however the difference in SPL for the thinnest aerofoil (6%) at the highest mean flow speed (80ms^{-1}) is very small. We can summarise these results by returning to the factor, k^*R_e/U^*; greater values of k^*R_e/U^* produce greater noise reductions.

We compare the experimental results of Figures 7(a)–(h) to the analytical results in Figure 8, which plot the far-field acoustic directivity for low Mach number flow ($M = 0.06, 0.24$) at two different frequencies $k = 2.5, 5$. The directivity, $D(\theta)$, is defined in (2.29), and is restricted in Figure 8 to the experimentally measured range, $\theta \in [40°, 140°]$.

Analytically we focus on gusts with zero spanwise wavenumber, $k_3 = 0$ and $A_3 = 0$, since the experimental setup is fundamentally two dimensional. The dominant contributor to leading-edge noise for symmetric aerofoils in homogeneous isotropic turbulence

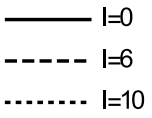

Figure 6: Legend for experimental and analytical results in Figures 7 and 8, with I defined in (3.1). The corresponding values of m can be found in Table 1 for aerofoil thicknesses of 6% and 12%.

arises from purely transverse disturbances ($k_n = A_n = 0$) (Gill *et al.* 2014) thus we take $k_n = 0$.

We require the gust to be solenoidal, therefore $A_t + A_n k_n \beta_\infty = 0$, and to ensure we ensure the magnitude of the incident gust vector far upstream is constant we set $A_t^2 + A_n^2 = 1$. Specifying k_n thus completely determines the incident gust.

We observe a good agreement between the experimental and analytical trends which overall indicate that an increased nose radius (blunter nose) reduces noise.

The analytical and experimental results agree well for $k = 5$, with the NACA 0006 indicating a linear reduction of noise with increasing nose radius, whilst the NACA 0012 results showing the $I = 10$ result can produce more noise that the $I = 6$.

The analytic $k = 2.5$ results show a weaker effect of altering nose radius on the noise produced, in agreement with the experimental measurements. The analytic results predict an increase of noise for a very blunt nose ($I = 10$) compared to a very sharp nose ($I = 0$) in the upstream direction ($\theta = \pi$ being the directly upstream direction) except for 6% thickness in the lowest speed flow, $M = 0.06$ (Figure 8(f)). This feature is only shown in the experimental results at the final upstream microphone location for the 12% aerofoils. We note the analytic results neglect transition regions which heavily influence an $O(k^{-1/2})$ polar angle region directly upstream and downstream (Ayton 2016). This is equivalent to an angle of 36°, thus we would expect potential inaccuracies at the extremities of the analytic results for $k = 2.5$. Further, the amplitude errors elsewhere in the analytic solution are $O(k^{-1})$ as we assume $k \gg 1$. Thus we expect bigger errors in the lower frequency analytic results than the higher frequency analytic results. We also see a difference in overall pattern between the analytically predicted SPL for $k = 2.5$, $M = 0.06$ - the analytic results do not decrease with increasing θ. We also attribute this to a lack of inclusion of a transition region for the larger θ values.

4.2. *Mechanisms for noise generation*

Having determined the trends experimentally for increasing nose radius we see good agreement to the analytical solution. We now use our analytical leading-edge solution, (2.21), to investigate the individual flow features that could impact the change of noise generation when nose radius is altered. We do so by considering the individual terms in the leading-edge solution given by $L_{1,2,3c_{1,2,3},3p}(\theta)$ as each describes a different physical process occurring in the governing equations.

We previously considered only $k_n = 0$, however to get a full picture of the effects of all leading-edge terms we shall consider two cases here, $k_n = 0, 1$. We also wish to determine the effects of higher Mach number flow, which are practically relevant to the leading-edge noise problem, but due to facility restrictions could not be investigated experimentally.

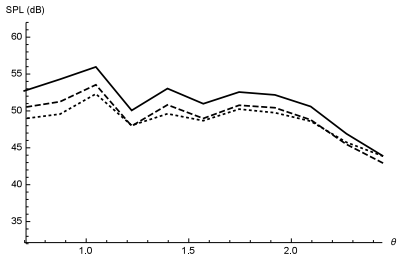

(a) NACA 0012, $M = 0.24$, $k = 2.5$.

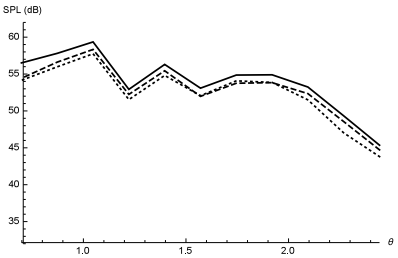

(b) NACA 0006, $M = 0.24$, $k = 2.5$.

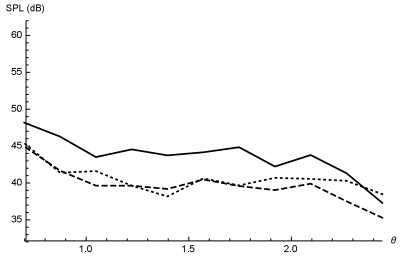

(c) NACA 0012, $M = 0.24$, $k = 5$.

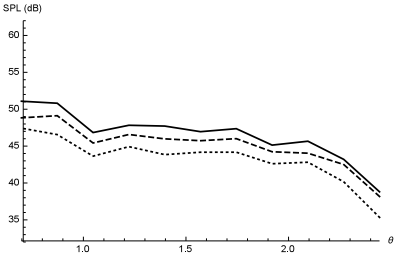

(d) NACA 0006, $M = 0.24$, $k = 5$.

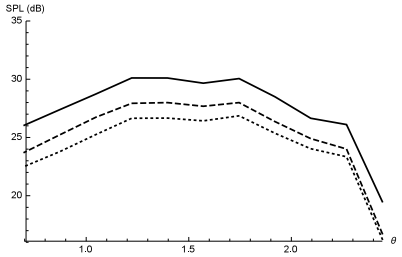

(e) NACA 0012, $M = 0.06$, $k = 2.5$.

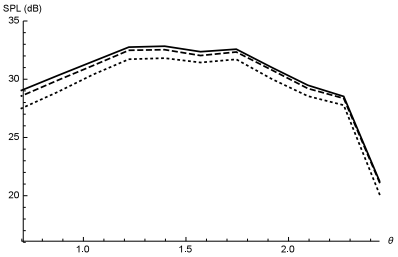

(f) NACA 0006, $M = 0.06$, $k = 2.5$.

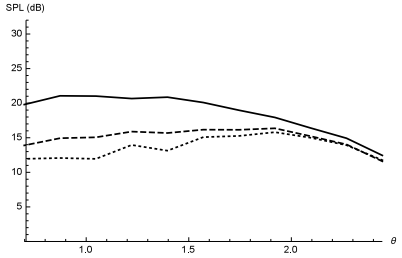

(g) NACA 0012, $M = 0.06$, $k = 5$.

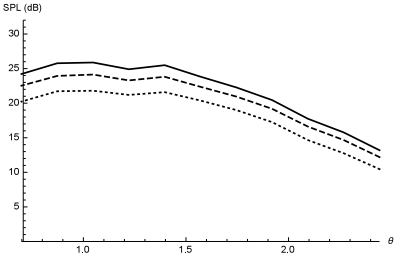

(h) NACA 0006, $M = 0.06$, $k = 5$.

Figure 7: Sound pressure level measured experimentally against polar angle θ. Legend given in Figure 6.

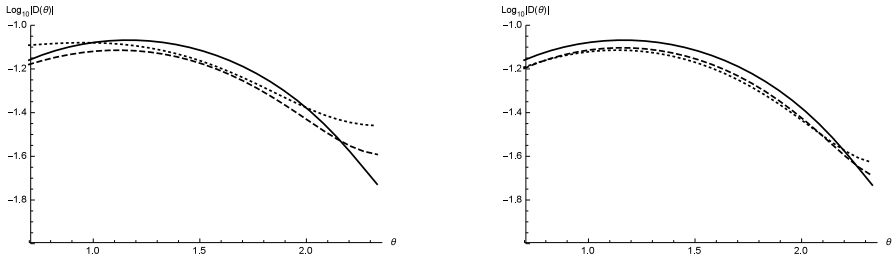

(a) NACA 0012, $M = 0.24$, $k = 2.5$.

(b) NACA 0006, $M = 0.24$, $k = 2.5$.

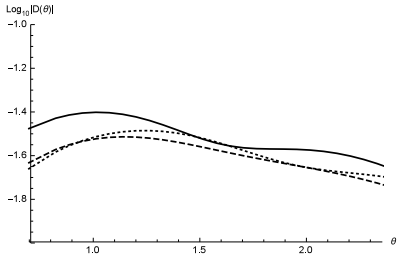

(c) NACA 0012, $M = 0.24$, $k = 5$.

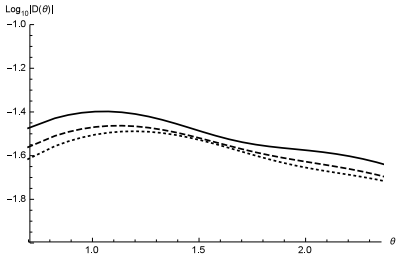

(d) NACA 0006, $M = 0.24$, $k = 5$.

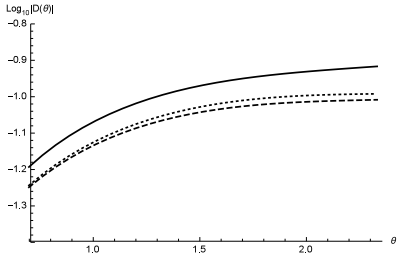

(e) NACA 0012, $M = 0.06$, $k = 2.5$.

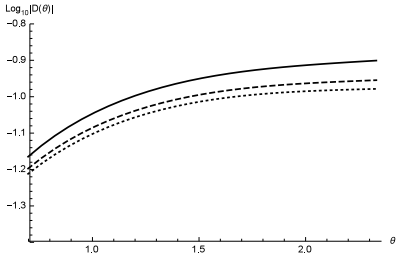

(f) NACA 0006,$M = 0.06$, $k = 2.5$.

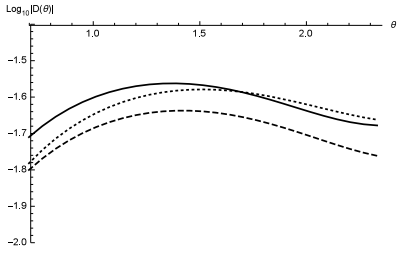

(g) NACA 0012, $M = 0.06$, $k = 5$.

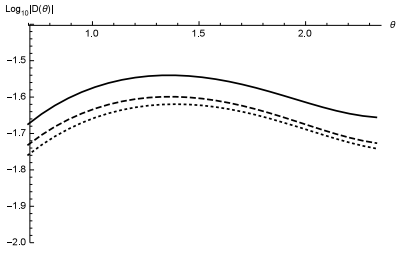

(h) NACA 0006, $M = 0.06$, $k = 5$.

Figure 8: Analytic far-field acoustic directivity, $\log_{10}|D(\theta)|$, against polar angle θ. Legend given in Figure 6.

We hence consider both low and high Mach number flows analytically, $M = 0.3, 0.6$. Finally, since a higher frequency leads to a greater difference in noise generation with varying nose radius, and the analytic results become increasingly accurate with increasing frequency, we shall focus on two high-frequency cases $k = 5, 10$.

We notice that k_n does not explicitly feature in the terms L_{3p,c_i} in the leading-edge solution (2.21), and A_n is an overall factor, since the H_3 solution considers the distortion of the flat-plate acoustics through a locally non-uniform flow at the nose - a process that

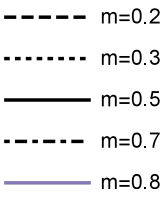

Figure 9: Legend for analytic results.

is independent of the gust. Therefore the effect of altering k_n on these terms will be an overall scaling factor only (since altering k_n alters the coefficient A_n). The main influence of k_n lies in the $L_{1,2}$ terms which represent the effects of the changing surface normal direction on blocking gust velocities, and effects of the volume source generated by the gust in the locally non-uniform flow at the nose, respectively. Both processes are clearly dependent on the gust normal wavevector component. We therefore present $|L_{1,2}|$ for both $k_n = 0, 1$, but $|L_{3p,c_{1,2,3}}|$ only for $k_n = 0$, in Figures 10 and 11 when $M_\infty = 0.6$, and $|L_{1,2,3p,3c_i}|$ for $k_n = 0$ at $M_\infty = 0.3$ in Figure 12. We consider five different leading-edge geometries, defined by $m = 0.2$, 0.3, 0.5, 0.7, 0.8, and all analytic plots share the legend shown in Figure 9.

In Figure 10 ($k_n = 0$, $M_\infty = 0.6$), Figure 11 ($k_n = 1$, $M_\infty = 0.6$) and Figure 12 ($k_n = 0$, $M_\infty = 0.3$) the scaling parameter $\epsilon a_0 k^{1-m}$ is neglected, therefore we have removed the thickness and frequency scaling of the locally non-uniform mean flow at the nose (which as m increases to give a sharper nose, reduces in magnitude). Having removed this asymptotic parameter, for each given m, the relative magnitude of the results in Figures 10, 11 and 12 indicate the level of influence of that term in the total leading-edge acoustic pressure. We see that by increasing m, the influence of $L_{3c_{1,2,3}}$ reduces, but the influence of $L_{2,3p}$ increases. This indicates that source terms (the volume source for L_2, and the flat-plate acoustics for L_{3p}) become more important as the leading edge is sharpened.

By considering the boundary condition for H_1, (2.15b), we see it consists of normal and tangential gust terms, $A_{n,t}$, multiplied by directional terms, $\sin(m\pi)$ and $\cos(m\pi)$. In the case of $k_n = 0$, the outer limit, L_1 shown in Figure 10a, has no tangential component ($A_t = 0$), thus the solution depends only on the (vertical) directional term $\sin(m\pi)$. The magnitude of L_1 hence varies proportionally to $|\sin(m\pi)|$ as m varies, thus unlike $L_{2,3}$ there is no trend of overall increase or decrease with increasing m. When $A_t \neq 0$ in Figure 11a, we see L_1 decreases in magnitude for increasing m. Here the variation in size of the directional terms $\sin(m\pi)$ and $\cos(m\pi)$ are less important, and the overall scaling in m arising from the Fourier transform of Φ^{m-1}, which represents the rate of slowing of the steady flow on approach to the frontal stagnation point, dominates. A smaller value of m indicates a blunter nose, therefore a greater rate of slowing of the flow and a larger magnitude of the solution L_1.

Figure 11b illustrates the effects of an asymmetric incident field on a symmetric aerofoil, as the gust distortion at the nose depends on the angle at which it approaches the aerofoil. The overall trend as m varies agrees with the symmetric $k_n = 0$ case in Figure 10b, indicating for $k_n \neq 0$ the volume source term is still promoted as m increases.

We now consider the magnitudes of the $L_{1,2,3p,3c_{1,2,3}}$ for low Mach number, $M_\infty = 0.3$, in Figure 12 and compare to the results for moderate Mach number, $M_\infty = 0.6$ (Figure 10). Overall all directivities are stretched horizontally for $M_\infty = 0.6$ compared to $M_\infty =$

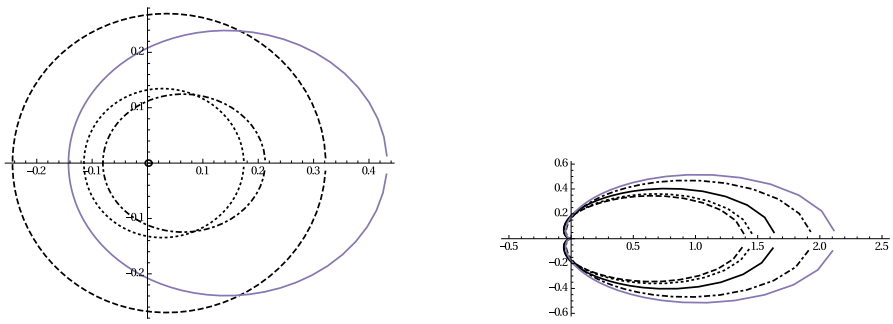

(a) $|L_1(\theta)|$

(b) $|L_2(\theta)|$

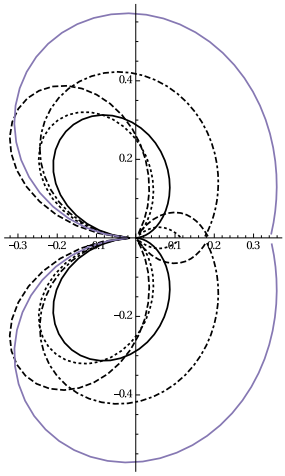

(c) $|L_{3p}(\theta)|$

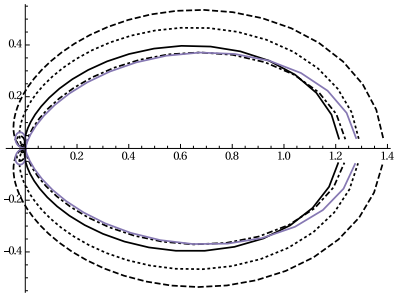

(d) $|L_{3c_1}(\theta)|$

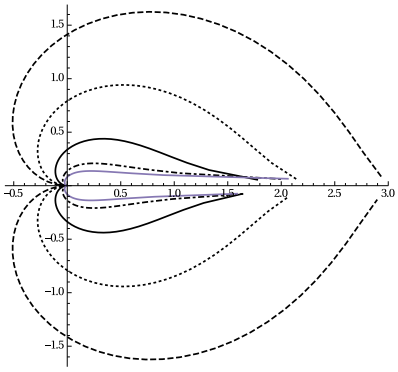

(e) $|L_{3c_2}(\theta)|$

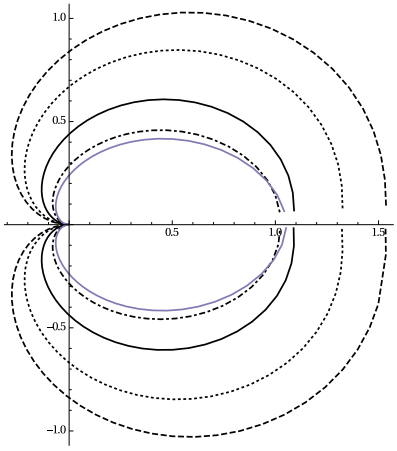

(f) $|L_{3c_3}(\theta)|$

Figure 10: Polar plot of $L_{1,2,3p,3c_{1,2,3}}$ for different leading-edge geometries, for $M_\infty = 0.6$, and $k_n = 0$. Legend given in Figure 9.

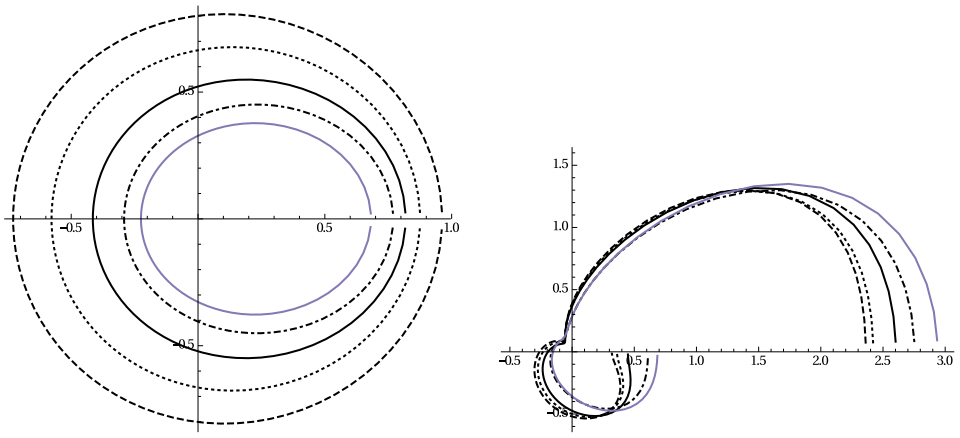

(a) $|L_1(\theta)|$ (b) $|L_2(\theta)|$

Figure 11: Polar plot of $L_{1,2}$ for different leading-edge geometries, for $M_\infty = 0.6$, and $k_n = 1$. Legend given in Figure 9.

m	a_0	$\epsilon a_0\, 5^{1-m}$	$\epsilon a_0\, 10^{1-m}$
0.2	0.567	0.123	0.215
0.3	0.683	0.126	0.205
0.5	1.000	0.134	0.190
0.7	1.517	0.147	0.182
0.8	1.933	0.160	0.184

Table 2: Table of values of m and a_0 chosen to ensure equal total aerofoil thickness $\epsilon = 0.06$ for a modified NACA 4-digit profile, and asymptotic parameter $\epsilon a_0 k^{1-m}$ with $k = 5, 10$.

0.3 due to Doppler effects, but trends when varying m for each individual directivity function remain the same. We also see that the relative sizes of certain $L_{1,2,3p,3c_{1,2,3}}$ are decreased; in particular, at low Mach number, $L_{1,3p}$ are substantially smaller than at moderate Mach number. Thus at low Mach number, and effects of $L_{1,3p}$ will be less evident in the total far-field acoustic solution than at moderate Mach number.

Finally we plot the full pressure directivity, $|D(\theta)|$, as given by (2.29). We focus specifically on $k_n = 0$ gusts. All aerofoils have the same maximum thickness, but varying leading-edge geometry, as can be seen in Figure 13, produced by taking the standard NACA-4 digit profile but altering the first term from $x^{0.5}$ to x^m. To ensure the maximum thickness is fixed across all aerofoils, different values of a_0 have to be chosen for different values of m. These are given in Table 2. We see from this table that the parameter, $\epsilon a_0 k^{1-m}$ is similar across the range of m chosen for our two chosen frequencies $k = 5, 10$, therefore any effects seen altering the far-field noise are not caused purely by the changing scaling of the steady flow at the nose, q (2.3).

Figure 14 gives the directivity for $k_n = 0$ and $M_\infty = 0.3$ at two gust frequencies, $k = 5, 10$; we see that as the aerofoil nose becomes blunter (decreasing m) the noise reduces across all angles for both frequencies (as also seen in Figure 8 for the comparison with

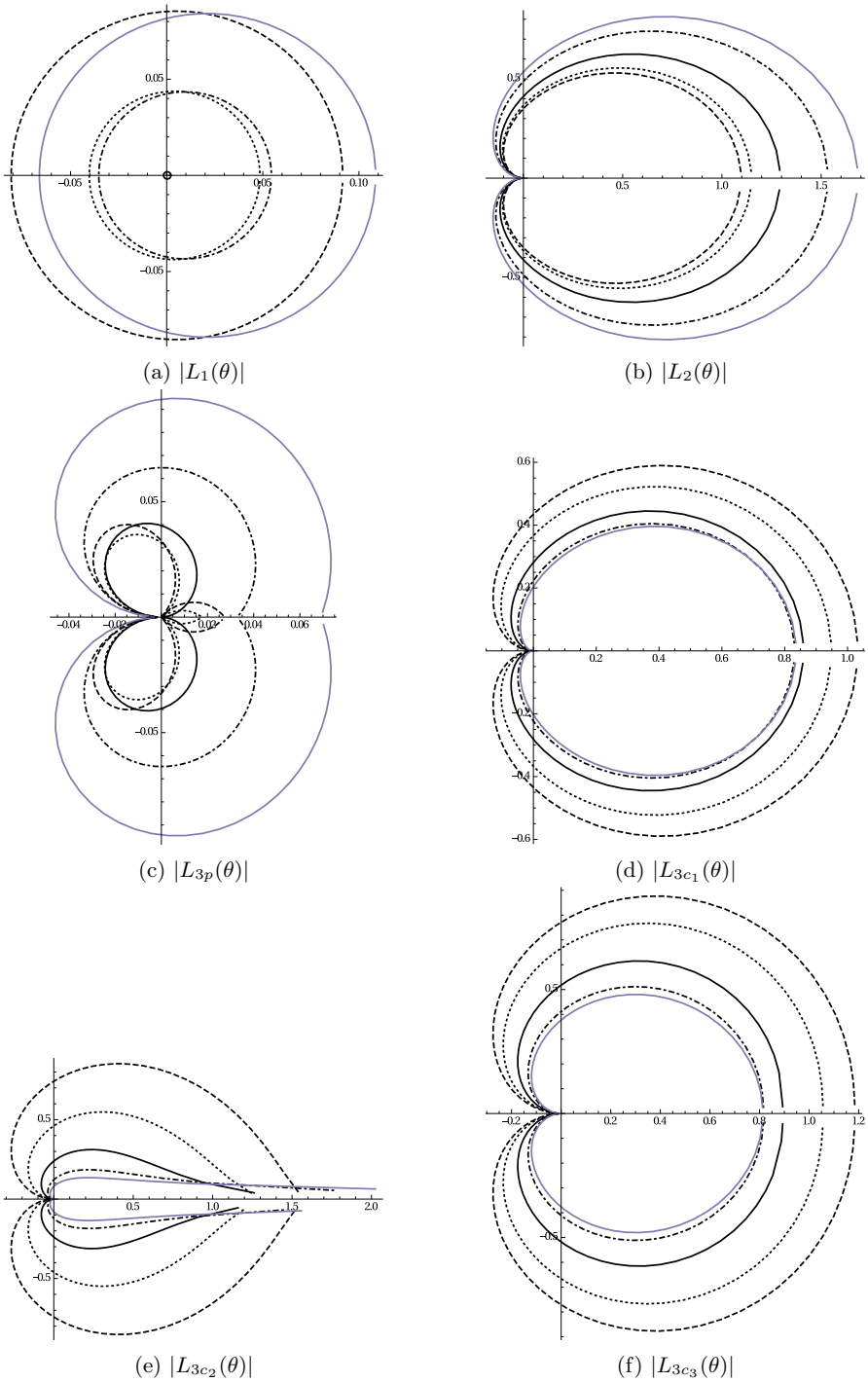

(a) $|L_1(\theta)|$ (b) $|L_2(\theta)|$

(c) $|L_{3p}(\theta)|$ (d) $|L_{3c_1}(\theta)|$

(e) $|L_{3c_2}(\theta)|$ (f) $|L_{3c_3}(\theta)|$

Figure 12: Polar plot of $L_{1,2,3p,3c_{1,2,3}}$ for different leading-edge geometries, for $M_\infty = 0.3$, and $k_n = 0$. Legend given in Figure 9.

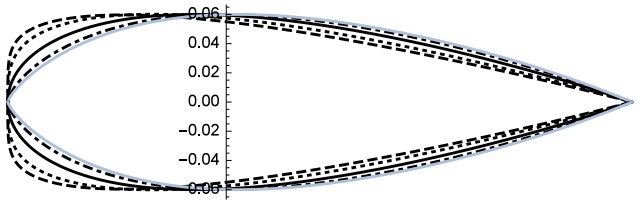

Figure 13: Full aerofoil shapes (with chord length 2) used for different leading-edge geometries $y \sim \epsilon a_0 x^m$. Legend given in Figure 9.

experimental data). To cause this we would expect source terms, indicated by solutions L_2 and L_{3p}, to add to the total noise, which is justified by the consistent trends seen in Figures 10c,10b and 14. Terms $L_{3c_{1,2,3}}$ likely subtract. We see similar results at frequency $k = 5$ as those seen at $k = 10$, since the only influence of the frequency on the directivity is in the asymptotic scaling parameter $\epsilon a_0 k^{1-m}$, which affects the total size of the added thickness-related terms, but not the individual effects seen by varying m in the $L_{1,2,3}$ terms.

At higher Mach number, $M_\infty = 0.6$, Figure 15 for frequencies $k = 5, 10$ shows more significant modulation of the solution, due to the greater interference between leading- and trailing-edge fields. At both frequencies we see an increase of noise in the upstream region for a very blunt leading edges ($m = 0.2$), although elsewhere the noise is reduced as m is decreased. This upstream increase was observed experimentally in Figure 7 for a 12% total thickness aerofoil in low Mach number flow. Analytically the upstream increase is greatest for $k = 10$. By increasing the Mach number we have increased the relative importance of terms $L_{1,3p}$. We can determine that the L_1 term subtracts from the flat-plate term, L_0, by considering the phase difference between L_1 and L_0. Therefore the rate of slowing of the flow on approach to the stagnation point decreases far-field noise. Since L_1 subtracts from the flat-plate term we do not expect this term to be contributing to the increase of noise upstream. Instead we notice that the L_{3p} term for $M_\infty = 0.6$ in Figure 10c shows an increase in magnitude in the upstream region as m is reduced, which is more extreme than the distortion to the upstream direction seen for $M_\infty = 0.3$ in Figure 12c. We therefore attribute the increase in noise upstream seen in Figure 15 to the increased upstream distortion seen in L_{3p} at higher Mach numbers, which as a source term adds to the total noise. Specifically, L_{3p} accounts for the distortion of the volume source generated by the flat-plate term due to the locally non-uniform mean flow around the nose. This locally non-uniform flow is directed upstream, and increases with the bluntness of the nose thus as we decrease m we see a distortion of the acoustics from L_{3p} to the upstream direction, that is increasingly evident at higher Mach numbers.

5. Conclusions

In this paper we have considered the effects of local aerofoil nose geometry on leading-edge noise, both analytically and experimentally. We have seen that increasing the nose radius (to create a blunter nose) reduces the far-field noise generated for a fixed overall thickness of aerofoil for high-frequency interactions at low Mach numbers. At higher Mach numbers the analytic solution predicts an increase of noise upstream for blunter aerofoils but a decrease downstream for blunter aerofoils. The analytic solution for the far-field acoustics is correct to two orders of magnitude in the amplitude and phase at all polar angles, $\theta > O(k^{-1/2})$. We have neglected the transition regions formally required

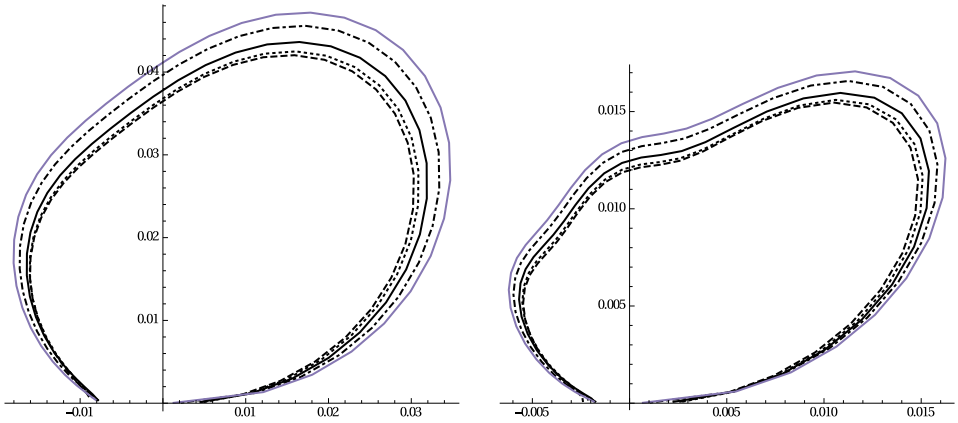

(a) $k = 5$ (b) $k = 10$

Figure 14: Polar plot of the far-field acoustic directivity, $|D(\theta)|$, for different leading-edge geometries, for $k_n = 0$, $M_\infty = 0.3$. Legend given in Figure 9.

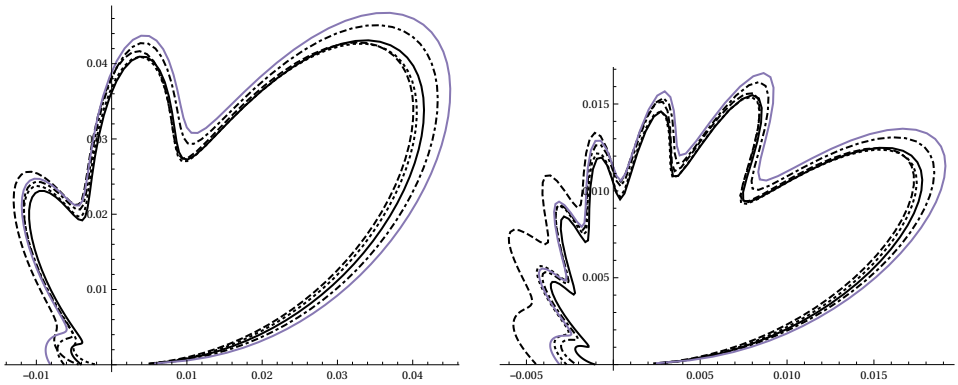

(a) $k = 5$ (b) $k = 10$

Figure 15: Polar plot of the far-field acoustic directivity, $|D(\theta)|$, for different leading-edge geometries, for $k_n = 0$, $M_\infty = 0.6$. Legend given in Figure 9.

for a full matched asymptotic solution and accuracy across all observer angles since these transition solutions only have an effect at small downstream angles, $\theta = O(k^{-1/2})$.

The analytic solution, which extends previous analytic work for parabolic leading edges, qualitatively agrees with the experimental findings, and has been used to understand the reasons behind the noise generated by different leading-edge geometries. Importantly, it is not just the overall steady flow speed near the nose (the asymptotic scaling parameter $\epsilon a_0 k^{1-m}$) that has an effect on the total noise; we have seen that volume sources are promoted for sharper leading edges, increasing noise, and the greater the rate of slowing of the steady velocity on approach to the nose the lower the overall sound levels. There is also a difference in the importance of acoustic generation mechanisms between low or moderate Mach numbers; the volume source term and horizontal blocking term are substantially smaller than other terms at low Mach numbers ($M_\infty = 0.3$), but are comparable with other terms at moderate Mach number ($M_\infty = 0.6$). At moderate Mach

numbers, the analytic solution predicts a blunter leading edge can increase far-field noise in the upstream direction for high-frequency gusts. This upstream increase has also been observed when increasing total aerofoil thickness in the numerical results of Lockard & Morris (1998) at $M_\infty = 0.5$.

Aerofoil thickness remains the main geometric parameter controlling turbulence interaction noise (shown previously). Local leading-edge geometry, such as nose radius, nevertheless is an important parameter for thin aerofoils at high frequencies, particularly when the gust wavelength is comparable to nose radius. Therefore attempts to predict interaction noise based on single values of thickness-chord ratio, ϵ, and frequency, k, are likely to be inaccurate for thin aerofoils since nose-radius parameter, m, also plays a key role. The ability to reduce aerofoil interaction noise by increasing the nose radius but maintaining a constant overall thickness could be very useful for controlling aeroengine noise, where increasing blade thickness is not practical.

Acknowledgements

LA is grateful to Sidney Sussex College for providing financial support. PC is grateful to Prof. Phillip Joseph for supporting the experimental test campaign at ISVR, Southampton.

Appendix A. Outer limit of H_2 solution

Upon evaluating the acoustic parts of $H_{2c,p}$ using the method of steepest descents, we obtained the outer limit as

$$H_2 \sim \frac{\mathrm{e}^{\mathrm{i}kwr}}{\sqrt{kr}} L_2(\theta), \tag{A.1}$$

where

$$\begin{aligned} L_2(\theta) = {} & \frac{-\mathrm{e}^{-\pi \mathrm{i} m/2}(1-\mathrm{e}^{2\pi \mathrm{i} m})\Gamma(m)\sqrt{2\pi w}|\sin\theta|\mathrm{e}^{-\pi \mathrm{i}/4}}{16\pi(1-m)(\delta^2+k_n^2)(\delta - w\cos\theta)^m(-w\cos\theta-\lambda_1)(-w\cos\theta-\lambda_2)} \\ & \left(\frac{(\delta - w\cos\theta)f_1(-w\cos\theta) + ik_n\, f_2(-w\cos\theta)}{\sqrt{(-w\cos\theta)^2 - w^2}} - \mathrm{sgn}(\Psi) f_2(-w\cos\theta)\right) \\ & - \frac{\mathrm{sgn}(\Psi)\mathrm{e}^{-\pi \mathrm{i} m/2}(1-\mathrm{e}^{2\pi \mathrm{i} m})\Gamma(m)\sqrt{2\pi w}|\sin\theta|\mathrm{e}^{-\pi \mathrm{i}/4}}{16\pi(1-m)(\delta^2+k_n^2)\sqrt{-w\cos\theta + w}} \left\{ 2(-\delta C_4 + k_n C_3)\mathcal{H}(\frac{1}{2} - m) \right. \\ & - \left(\frac{\sqrt{w + w\cos\theta} f_2(-w\cos\theta)}{(\delta - w\cos\theta)^m(-w\cos\theta - \lambda_2)} + \frac{\sqrt{\lambda_1 + w} f_2(\lambda_1)}{(\lambda_1+\delta)^m(\lambda_1 - \lambda_2)}\right) \frac{1}{-w\cos\theta - \lambda_1} \\ & \left. + \frac{(\lambda_2+\delta)f_2(\lambda_2) + ik_n f_1(\lambda_2)}{\sqrt{\lambda_2 - w}(\lambda_2 + \delta')^m(\lambda_2 + w\cos\theta)(-w\cos\theta - \lambda_1)} \right\}, \end{aligned} \tag{A.2}$$

with $\mathcal{H}$ denoting the Heaviside function.

Appendix B. Solution for H_{3c} and H_{3p}

Here we find the solution to (2.20). First, we evaluate the H_0 terms in the governing equation and boundary condition thus we must solve

$$D(H_3) = -\frac{A_n \mathrm{sgn}(\Psi) C w^2}{\beta_\infty \pi \sqrt{\delta + w}} \left(R^{m-1} \cos((1-m)\theta + m\pi) \int_\infty^\infty \left[\frac{1}{(\lambda+\delta)\sqrt{\lambda + w}} - \frac{(\gamma+1)M_\infty^4}{2\beta_\infty^4 w^2} \frac{\lambda+\delta}{\sqrt{\lambda+w}} \right] \mathrm{e}^{a(\lambda,\Phi,\Psi)} d\lambda + \frac{\mathrm{i}(\gamma+1)M_\infty^4}{2\beta_\infty^4 w^2} (1-m) R^{m-2} \cos((2-m)\theta + m\pi) \int_{-\infty}^\infty \frac{\mathrm{e}^{a(\lambda,\Phi,\Psi)}}{\sqrt{\lambda+\delta}} d\lambda \right) \tag{B.1}$$

$$\left. \frac{\partial H_3}{\partial \Psi} \right|_{\substack{\Phi>0 \\ \Psi=0\pm}} = -\frac{A_n M_\infty^2 C (1-m) \sin(m\pi)}{2\pi \beta_\infty^2 \sqrt{\delta + w} \Phi^{2-m}} \int_{-\infty}^\infty \frac{\mathrm{e}^{-\mathrm{i}\lambda\Phi}}{(\lambda+\delta)\sqrt{\lambda+w}} d\lambda \tag{B.2}$$

By considering a particular solution of the form

$$f(\theta) \int_{-\infty}^\infty B(\lambda) \mathrm{e}^{a(\lambda,\Phi,\Psi)} d\lambda, \tag{B.3}$$

with

$$f(\theta) = \left\{ R^{m-1} \cos((1-m)\theta + m\pi),\ R^{m-1} \sin((1-m)\theta + m\pi), \right. \\ \left. R^m \cos(-m\theta + m\pi),\ R^m \sin(-m\theta + m\pi) \right\}, \tag{B.4}$$

we can find appropriate $B(\lambda)$ functions to satisfy the forcing in the governing equation.

We obtain a particular solution

$$H_{3p} = -\frac{A_n \mathrm{sgn}(\Psi) C w^2}{\pi \sqrt{\delta + w}} \left[R^m \cos(-m\theta + m\pi) \int_{-\infty}^\infty \frac{\mathrm{i}\lambda}{2mw^2} \left(\frac{1}{(\lambda+\delta)\sqrt{\lambda+w}} - \frac{(\gamma+1)M_\infty^4}{2\beta_\infty^4 w^2} \frac{\lambda+\delta}{\sqrt{\lambda+w}} \right) \mathrm{e}^{a(\lambda,\Phi,\Psi)} d\lambda \right. \\ + R^m \sin(-m\theta + m\pi) \int_{-\infty}^\infty \frac{-\mathrm{sgn}(\Psi)}{2mw^2} \left(\frac{\sqrt{\lambda - w}}{\lambda+\delta} - \frac{(\gamma+1)M_\infty^4}{2\beta_\infty^4 w^2} \sqrt{\lambda - w}(\lambda+\delta) \right) \mathrm{e}^{a(\lambda,\Phi,\Psi)} d\lambda \\ + R^{m-1} \cos((1-m)\theta + m\pi) \int_{-\infty}^\infty \frac{(\gamma+1)M_\infty^4}{4\beta_\infty^4 w^4} \frac{\lambda}{\sqrt{\lambda+w}} \mathrm{e}^{a(\lambda,\Phi,\Psi)} d\lambda \\ \left. + R^{m-1} \sin((1-m)\theta + m\pi) \int_{-\infty}^\infty \frac{\mathrm{i}\,\mathrm{sgn}(\Psi)(\gamma+1)M_\infty^4}{4\beta_\infty^4 w^4} \sqrt{\lambda - w} \mathrm{e}^{a(\lambda,\Phi,\Psi)} d\lambda \right]. \tag{B.5}$$

This solution, like that for the parabolic leading edge, is singular as $R \to 0$ which is not a permitted solution of the governing equation. To correct this singularity, we introduce a homogeneous solution that has the required small R behaviour to cancel the singularity. This process is very similar to that in Tsai (1992) and therefore not repeated here. We

find the additional solution we must include is

$$H^c_{3p} = \frac{A_n C\sqrt{\pi}\mathrm{e}^{\pi\mathrm{i}/4}}{m\sqrt{\delta+w}}\frac{(\gamma+1)M_\infty^4}{8\beta_\infty^4 w^2}\left[\frac{\mathrm{i}(2m-3)Ha_{\frac{5}{2}-m}(w\Phi)\cos((\frac{5}{2}-m)\theta+m\pi)}{\Gamma(\frac{5}{2}-m)}\left(\frac{w}{2}\right)^{\frac{5}{2}-m}\right.$$
$$\left.-\frac{(-2\delta+w-2mw)Ha_{\frac{3}{2}-m}(w\Phi)\cos((\frac{3}{2}-m)\theta+m\pi)}{\Gamma(\frac{3}{2}-m)}\left(\frac{w}{2}\right)^{\frac{3}{2}-m}\right], \tag{B.6}$$

where Ha are Hankel functions of the first kind.

We now require a complementary solution to (B.1) that satisfies

$$\left.\frac{\partial H_{3c}}{\partial\Psi}\right|_{\substack{\Phi>0\\Psi=0\pm}} = -\frac{A_n M_\infty^2 C(1-m)\sin(m\pi)}{2\pi\beta_\infty^2\sqrt{\delta+w}\Phi^{2-m}}\int_{-\infty}^{\infty}\frac{\mathrm{e}^{-\mathrm{i}\lambda\Phi}}{(\lambda+\delta)\sqrt{\lambda+w}}d\lambda - \left.\frac{\partial H_{3p}}{\partial\Psi}\right|_{\substack{\Phi>0\\Psi=0\pm}} - \left.\frac{\partial H^c_{3p}}{\partial\Psi}\right|_{\substack{\Phi>0\\Psi=0\pm}}. \tag{B.7}$$

Analogously to the parabolic case can write the boundary condition as

$$\left.\frac{\partial H_{3c}}{\partial\Psi}\right|_{\substack{\Phi>0\\Psi=0\pm}} = d_1(\Phi)+d_2(\Phi)+d_3(\Phi), \tag{B.8}$$

and define $H_{3c} = H_{3c_1}+H_{3c_2}+H_{3c_3}$ so that H_{3c_i} satisfies the d_i term in the boundary condition.

The d_i are defined as

$$d_1(\Phi) = \frac{2A_nC\beta_\infty}{\sqrt{\delta^2-w^2}}\sin(m\pi)\mathrm{e}^{\mathrm{i}\delta\Phi}\left(\mathrm{i}\delta\Phi^{m-1}-\frac{1}{m}(\delta^2-w^2)\Phi^m\right) \tag{B.9}$$

$$d_2(\Phi) = \frac{2A_nC\beta_\infty w}{\sqrt{\pi}\sqrt{\delta+w}(\delta-w)}\left(\frac{1}{m}-1\right)\mathrm{e}^{\pi\mathrm{i}/4+\mathrm{i}w\Phi}\sin(m\pi)\left(1-\frac{(\gamma+1)M_\infty^4}{2\beta_\infty^4w^2}(\delta-w)^2\right)\frac{1}{\Phi^{\frac{3}{2}-m}} \tag{B.10}$$

$$\begin{aligned}
d_3(\Phi) = {} & \frac{A_nC\beta_\infty}{\sqrt{\pi}\sqrt{\delta+w}}\sin(m\pi)\mathrm{e}^{\mathrm{i}w\Phi}\left\{\sqrt{\pi}\mathrm{e}^{-3\pi\mathrm{i}/4}\Phi^{m-\frac{3}{2}}\left[\left(\frac{1}{m}-2\right)-\frac{2\mathrm{i}}{m}(\delta-2w)\Phi\right]\right.\\
& +\sqrt{\pi}\frac{(\gamma+1)M_\infty^4}{2\beta_\infty^4w^2}\mathrm{e}^{\pi\mathrm{i}/4}\Phi^{m-1}\left[\left(4-\frac{15}{4m}-m\right)\frac{1}{\Phi^{\frac{5}{2}}}\right.\\
& \left.\left.+\mathrm{i}\left(-6w+\frac{9w}{2m}+2mw+\delta-\frac{3\delta}{2m}\right)\frac{1}{\Phi^{\frac{3}{2}}}\right]\right\}\\
& -\frac{2A_nC\beta_\infty w}{\sqrt{\pi}\sqrt{\delta+w}(\delta-w)}\left(\frac{1}{m}-1\right)\mathrm{e}^{\mathrm{i}w\Phi+\pi\mathrm{i}/4}\frac{\sin(m\pi)}{\Phi^{\frac{3}{2}-m}}\\
& -\frac{A_nC\beta_\infty}{\sqrt{\delta^2-w^2}}\sin(m\pi)\mathrm{e}^{\mathrm{i}\delta\Phi}\left[\mathrm{i}\delta\Phi^{m-1}-\frac{1}{m}(\delta^2-w^2)\Phi^m\right]\mathrm{erfc}\left(\mathrm{e}^{\pi\mathrm{i}/4}\sqrt{(\delta-w)\Phi}\right)\\
& +\frac{A_nM_\infty^2C}{\beta_\infty\sqrt{\delta^2-w^2}}\frac{\sin(m\pi)}{\Phi^{2-m}}\mathrm{e}^{\mathrm{i}\delta\Phi}\mathrm{erf}\left(\mathrm{e}^{\pi\mathrm{i}/4}(\delta-w)\Phi\right)\\
& +\frac{2A_nC\beta_\infty\sqrt{\pi}\mathrm{e}^{\pi\mathrm{i}/4}}{\sqrt{\delta+w}m}\frac{(\gamma+1)M_\infty^4}{8\beta_\infty^4w^2}\frac{\sin(m\pi)}{\Phi}\left[\frac{-\mathrm{i}(\frac{5}{2}-m)(2m-3)}{\Gamma(\frac{5}{2}-m)}Ha_{\frac{5}{2}-m}(w\Phi)\left(\frac{w}{2}\right)^{\frac{5}{2}-m}\right.\\
& \left.+\frac{(\frac{3}{2}-m)(-2\delta+w-2mw)}{\Gamma(\frac{3}{2}-m)}Ha_{\frac{3}{2}-m}(w\Phi)\left(\frac{w}{2}\right)^{\frac{3}{2}-m}\right].
\end{aligned} \tag{B.11}$$

The solutions for H_{3c_i} are then give by

$$H_{3c_i} = \frac{-\mathrm{sgn}(\Psi)}{2\pi} \int_{-\infty}^{\infty} F_{+i}(\lambda) \frac{\mathrm{e}^{a(\lambda,\Phi,\Psi)}}{\sqrt{\lambda+\delta}} d\lambda, \tag{B.12}$$

where

$$F_{+i}(\lambda) = \frac{1}{2\pi\mathrm{i}} \int_{C_+} \frac{d\kappa}{\sqrt{\kappa-w}(\kappa-\lambda)} \int_0^{\infty} d_i(x) \mathrm{e}^{\mathrm{i}\kappa x} dx, \tag{B.13}$$

and C_+ is a contour parallel to but slightly above the real line.

The outer limits of H_{3c_i} are

$$H_{3c_i} \sim L_{3c_i}(\theta) \frac{\mathrm{e}^{\mathrm{i}kwr}}{\sqrt{kr}}, \tag{B.14}$$

where

$$L_{3c_i} = -F_{+i}(-w\cos\theta)\mathrm{sgn}(\theta)\cos\frac{\theta}{2} \frac{\mathrm{e}^{-\pi\mathrm{i}/4}}{\sqrt{\pi}}. \tag{B.15}$$

As with the parabolic leading-edge case, L_{3c_2} is singular at $\theta = 0$, indicating the need for a uniformly valid far-field expansion of H_{3c_2} for small θ values. The leading-edge transition solution then exists in this region of small θ values and acts to ensure the (total) normal velocity along the whole rigid aerofoil surface is zero. These two features only take effect for small θ values, and since we do not calculate the transition solution, we shall not calculate a uniformly valid expansion of H_{3c_2} here.

REFERENCES

Ayton, L. J., Gill, J. R. & Peake, N. 2016 The Importance of the unsteady Kutta condition when modelling gust-aerofoil interaction. *Journal of Sound and Vibration* **378**, 28–37.

Ayton, L. J. 2016 An analytic solution for gust-aerofoil interaction noise including effects of geometry. *IMA Journal of Applied Mathematics* **00**, 1–25.

Bender, C. M. & Orszag, S. A. 1978 *Advanced Mathematical Methods for Scientists and Engineers*. McGraw-Hill, New York, NY, USA, 1978.

Chong, T. P., Joseph, P. F. & Davis, P. O. A. L. 2008 A parametric study of passive flow control for a short, high area ratio 90° curved diffuser. *Journal of Fluids Engineering* **130**, 111104–12.

Allampalli, V., Hixon, R., Nallasamy, M. & Sawyer, S. D. 2009 High-accuracy large-step explicit Runge-Kutta (HALE-RK) schemes for computational aeroacoustics. *Journal of Computational Physics* **228**, 3837–3850.

Chaitanya, P., Gill, J., Narayanan, S., Joseph, P., Vanderwel, C., Zhang, X., & Ganapathisubramani, B. 2015 Aerofoil geometry effects on turbulence interaction noise. *21st AIAA/CEAS Aeroacoustics Conference, Dallas, TX* .

Amiet, R. K. 1975 Acoustic radiation from an airfoil in a turbulent stream. *Journal of Sound and Vibration* **41**, 407–420.

Crighton, D G 1985 The Kutta condition in unsteady flow. *Annual Review of Fluid Mechanics* **17**, 411–445.

Devenport, W. J., Staubs, J. K., & Glegg, S. A. L. 2010 Sound radiation from real airfoils in turbulence. *Journal of Sound and Vibration* **329**, 3470–3483.

Glegg, S. A. L. & Devenport, W. 2009 Unsteady loading on an airfoil of arbitrary thickness. *Journal of Sound and Vibration* **319**, 1252-1270.

Gill, J., Zhang, X., & Joseph, P. 2014 Reduced Dimension Modeling of Leading Edge Turbulent Interaction Noise. *20th AIAA/CEAS Aeroacoustics Conference, Atlanta, GA* .

Gill, J., Zhang, X., & Joseph, P. 2013 Symmetric airfoil geometry effects on leading edge noise. *Journal of the Acoustic Society of America* **134** 2669–2680.

Goldstein, M. E. 1978 Unsteady vortical and entropic distortions of potential flows round arbitrary obstacles. *Journal of Fluid Mechanics* **89**, 433–468.

Grace, S. M. 2001 Unsteady blade response: the BVI model vs. the gust model. *7th AIAA/CEAS Aeroacoustics Conference, Maastricht*.

Hall, A. M., Atassi, O. V., & Gilson, J. 2011 Effects of leading-edge thickness on high-speed aerofoil-turbulence interaction noise. *17th AIAA/CEAS Aeroacoustics Conference, Portland, Oregon*.

Hinze, J. O. 1959 Turbulence. McGraw-Hill.

Lockard, D. P. & Morris, P. J. 1998 Radiated noise from airfoils in realistic mean flows. *AIAA Journal* **36**, 907–914.

Myers, M. R. & Kerschen, E. J. 1995 Influence of incidence angle on sound generation by airfoils interacting with high-frequency gusts. *Journal of Fluid Mechanics* **292**, 271–304.

Myers, M. R. & Kerschen, E. J. 1997 Influence of camber on sound generation by airfoils interacting with high-frequency gusts. *Journal of Fluid Mechanics* **353**, 221–259.

S. Narayanan and P. Chaitanya and S. Haeri and P. Joseph and J. W. Kim and C. Polacsek 2015 Airfoil noise reductions through leading edge serrations. *Physics of Fluids* **27**.

Peake, N. & Parry, A. B. 2012 Modern challenges facing turbomachinery aeroacoustics. *Annual Review of Fluid Mechanics* **44**, 227–248.

Roach, P. E. 1987 The generation of nearly isotropic turbulence by mean of grid. *International Journal of Heat and Fluid Flow* **8**, 82–92.

Sears, W. R. 1941 Some aspects of non-stationary airfoil theory and its practical applications. *J. Aeron. Sci.* **8**, 104–188.

Olsen, W., & Wagner, J. 1982 Effect of Thickness on Airfoil Surface Noise. *AIAA Journal* **20**, 437–439.

Thwaites, B. 1960 *Incompressible aerodynamics: an account of the theory and observation of the steady flow of incompressible fluid past aerofoils, wings, and other bodies*. Dover Publications.

Tsai, C-T. 1992 Effect of Airfoil Thickness on High-Frequency Gust Interaction Noise. PhD thesis, University of Arizona.

Van Dyke, M. 1975 *Perturbation methods in fluid mechanics*. Parabolic Press.